RESEARCH ARTICLE

A potential vorticity budget view of the atmospheric circulation climatology over the Tibetan Plateau

Yongkun Xie[1] | Guoxiong Wu[2,3] | Yimin Liu[2,3] | Jianping Huang[1] |
Chen Sheng[2,3] | Yao Wu[2,3]

[1]Collaborative Innovation Center for Western Ecological Safety, Lanzhou University, Lanzhou, China

[2]State Key Laboratory of Numerical Modeling for Atmospheric Sciences and Geophysical Fluid Dynamics (LASG), Institute of Atmospheric Physics, Chinese Academy of Sciences, Beijing, China

[3]College of Earth and Planetary Sciences, University of Chinese Academy of Sciences, Beijing, China

Correspondence
Guoxiong Wu,
Email: gxwu@lasg.iap.ac.cn

Abstract

To aid the understanding of atmospheric circulation climatology over the Tibetan Plateau (TP), this study investigated the comprehensive potential vorticity (PV) budget over the TP using model-level reanalysis data. Our findings demonstrate the effects of diabatic heating, friction, gravity wave drag, advection, and convection in determining circulation over the TP, from the PV budget perspective. In summer, the diabatic heating-generated positive (negative) PV tendency facilitates cyclonic (anticyclonic) circulation near the surface (in the middle troposphere). Low PV in the upper troposphere, pertaining to the Asian monsoon anticyclone and monsoonal overturning circulation is induced by the upward transportation of diabatic heating-generated low PV in the middle troposphere. Horizontal advection further spreads the low PV—that is vertically inputted from the middle troposphere—to a wide area around the TP in the upper troposphere. In winter, the diabatic heating-generated positive PV near the surface is balanced by the sinking motion-carried low PV. In addition, gravity wave drag-generated PV is prominent in the upper troposphere in winter and can affect the downstream climate through advection. We further revealed the crucial role of the diurnal cycle in shaping the near-surface cyclonic circulation in summer by regulating the vertical structure of diabatic heating.

KEYWORDS

atmospheric circulation, diabatic heating, potential vorticity, Tibetan Plateau

1 | INTRODUCTION

Potential vorticity (PV) has been recognized as the basis for understanding various aspects of atmospheric dynamics since it was first proposed (Rossby, 1936; Ertel, 1942). PV exhibits its usefulness through its conceptual insights, such as isentropic PV maps and "PV thinking" (Hoskins *et al*., 1985). PV also has advantages in formulaic derivation and theoretical model construction (Charney and Stern, 1962; McIntyre, 2015). In addition, some diagnostic methods based on PV, such as the PV-based intrusion index (Cai, 2003; Škerlak *et al*., 2015), PV budget analysis (Büeler and Pfahl, 2017; Adames and Ming, 2018; Attinger *et al*., 2021), PV inversion (Davis and Emanuel, 1991; Xie *et al*., 2020), and PV-framework omega equation (Hoskins *et al*., 2003; Wu *et al*., 2020) are widely used.

The Tibetan Plateau (TP) has a large-scale topography and is located in the subtropics. TP topography influences general atmospheric circulation through mechanical and thermal forcing (Yeh, 1950; Manabe and Terpstra, 1974; Wu, 1984; Held and Ting, 1990). Circulation over the TP has strong seasonality. In summer, the ascending motion is accompanied by convergent flow and low pressure near the surface (Yeh, 1950; Yanai and Wu, 2006). In addition, Asian monsoon anticyclone (or South Asian high), with low PV, occupies the upper troposphere and lower stratosphere southwest of the TP (Hoskins and Rodwell, 1995; Garny and Randel, 2013; Amemiya and Sato, 2020). In winter, a sinking motion accompanies a divergent flow near the surface. Furthermore, the deflection effect of the TP topography on the westerlies is prominent in winter, when the westerlies are strong (Held and Ting, 1990; Wu et al., 2007).

Investigations using PV dynamics have yielded insights into the effects of the TP on the surrounding general atmospheric circulation. In particular, the mechanically forced circulation anomaly due to TP topography can be represented by the Rossby wave owing to the mechanically forced redistribution of PV (Hoskins et al., 1985; Held and Ting, 1990; Son et al., 2019). The thermally forced circulation anomaly caused by diabatic heating was characterized by the monsoonal overturning circulation (rising from the south TP and sinking to the Indian Ocean) and Asian monsoon anticyclone (Plumb and Hou, 1992; Hoskins and Rodwell, 1995). Several prominent centres of diabatic heating have been observed in summer, around the Asian summer monsoon region (Wu and Liu, 2003). The strongest diabatic heating is located over the Indian Ocean due to the northward migration of the intertropical convergence zone in summer (Schneider et al., 2014). The other three centres of diabatic heating were related to the South Asian (or Indian) summer monsoon, East Asian summer monsoon, and TP heating.

According to Plumb and Hou (1992), diabatic heating in the subtropics can induce a meridional circulation cell (angular momentum-conserving type) when the absolute vorticity vanishes at the upper boundary of the heating. The rising branch of the monsoonal overturning circulation in the Asian summer monsoon region extends further north (up to the TP) than the intertropical convergence zone. Therefore, the diabatic heating of the Asian summer monsoon and TP is crucial for the observed monsoonal overturning circulation because it generates the upper-level absolute vorticity minimum of the Asian monsoon anticyclone. The upper-level absolute vorticity minimum corresponds to a low PV (Hoskins, 1991). Studies have demonstrated that diabatic heating over the TP leads to the northward extension of the South and East Asian summer monsoons and facilitates the upper-level low PV

(Wu et al., 2012, 2016). Regarding the zonal location, the Asian monsoon anticyclone is located west of the total diabatic heating over the Asian summer monsoon regions. The zonal location is anchored by the phase relation between the temperature and vertical gradient of diabatic heating, under thermal wind approximation, and a relation that meridional advection of planetary vorticity is balanced by vorticity generation owing to the vertical gradient of diabatic heating, as a simplification of PV tendency equation (Wu et al., 2015a). In addition to climatology, the temporal variability of the Asian monsoon anticyclone has been explained by eddy shedding of the low PV (Hsu and Plumb, 2000; Rupp and Haynes, 2021).

Although studies have investigated the atmospheric circulation climatology and temporal variability over the Asian monsoon regions via PV dynamics, a comprehensive PV budget analysis from the Earth's surface to the upper atmosphere over the TP is lacking. For example, numerical simulations have demonstrated the effects of diabatic heating over the TP, on an upper-level low PV (Wu et al., 2016; Liu et al., 2017). However, specific processes concerning the Lagrangian non-conservative generation (diabatic heating, friction, and gravity wave drag) and Lagrangian conservative redistribution (advection and convection) of the PV have not been addressed. Note that the Lagrangian conservative redistribution is not conserved for a specific location in the Eulerian view. Therefore, all five processes (diabatic heating, friction, gravity wave drag, advection, and convection) can modify the local PV in the Eulerian view. By investigating the three-dimensional PV budget balanced through these multiple processes, this study aimed at gaining insight into the formation of circulation climatology over the TP.

The remainder of this paper is organized into three sections. Details of the data and methods are introduced in Section 2. The results are presented in Section 3: Section 3.1 addresses the general characteristics of climatological PV over the TP and its configuration with atmospheric circulation, Section 3.2 elaborates on how the multiple processes of non-conservative generation and conservative redistribution determined the balanced PV budget, and Section 3.3 further addresses the mechanisms of the formation of circulation climatology over the TP from a PV budget perspective. Conclusions and discussion are presented in Section 3.2.

2 | DATA AND METHODS

Since a lot of variables were examined in this study, a full list of the symbols and abbreviations of the variables is shown in Table 1. The symbols of the variables follow the APPENDICES in the textbook by Holton (2004).

TABLE 1 List of symbols and abbreviations, in order of the first appearance in the text

Symbols and abbreviations	Physical meaning	Unit
P, PV	Potential vorticity, Equation (1)	$K \cdot kg^{-1} \cdot m^2 \cdot s^{-1}$
$\dot{\theta}_{SW}$	Diabatic heating due to shortwave solar radiation	$K \cdot s^{-1}$
$\dot{\theta}_{LW}$	Diabatic heating due to longwave radiation	$K \cdot s^{-1}$
$\dot{\theta}_{SC}$	Diabatic heating due to shallow convection	$K \cdot s^{-1}$
$\dot{\theta}_{DC}$	Diabatic heating due to deep convection	$K \cdot s^{-1}$
$\dot{\theta}_{LC}$	Diabatic heating due to large-scale condensation	$K \cdot s^{-1}$
$\dot{\theta}_{VD}$	Diabatic heating due to vertical diffusion	$K \cdot s^{-1}$
ρ	Density	$kg \cdot m^{-3}$
$\boldsymbol{\omega}$	Three-dimensional absolute vorticity vector	s^{-1}
θ	Potential temperature	K
$\boldsymbol{\nabla}$	Three-dimensional gradient operator	N/A
$\boldsymbol{U} = (u, v, w)$	Three-dimensional wind velocity vector	$m \cdot s^{-1}$
W, PVD	PV density, Equation (2)	$K \cdot m^{-1} \cdot s^{-1}$
W_h	A component of PVD relating to the vertical shear of horizontal wind and horizontal gradient of potential temperature, Equation (2)	$K \cdot m^{-1} \cdot s^{-1}$
W_v	A component of PVD relating to the vertical component of absolute vorticity and vertical gradient of potential temperature, Equation (2)	$K \cdot m^{-1} \cdot s^{-1}$
f	Coriolis parameter, that is, the vertical component of planetary vorticity	s^{-1}
ζ	Vertical component of relative vorticity	s^{-1}
p	Pressure	Pa
g	Magnitude of gravity	$m \cdot s^{-2}$
$\boldsymbol{V_g} = (u_g, v_g)$	Geostrophic wind vector ($\equiv f^{-1} \boldsymbol{k} \times \boldsymbol{\nabla}\Phi$ in isobaric coordinates)	$m \cdot s^{-1}$
$\boldsymbol{k}$	Unit vector along the z-axis	N/A
Φ	Geopotential	$m^2 \cdot s^{-2}$
$\boldsymbol{\nabla}_h$	Horizontal gradient operator	N/A
TEND	Local tendency of PVD, Equation (4)	$K \cdot m^{-1} \cdot s^{-2}$
ADVE	Horizontal advective redistribution of PVD, Equation (4)	$K \cdot m^{-1} \cdot s^{-2}$
CONV	Vertical convective redistribution of PVD, Equation (4)	$K \cdot m^{-1} \cdot s^{-2}$
DIAB	Diabatic heating-generated PVD, Equation (4)	$K \cdot m^{-1} \cdot s^{-2}$
FRIC	Friction-generated PVD, Equation (4)	$K \cdot m^{-1} \cdot s^{-2}$
$\boldsymbol{V} = (u, v)$	Horizontal wind velocity vector	$m \cdot s^{-1}$
ω_{ml}	Vertical velocity for model-level data that was modified according to the vertical coordinate transformation rules, Equation (5)	$Pa \cdot s^{-1}$
ω	Vertical velocity in isobaric coordinates	$Pa \cdot s^{-1}$
$\dot{\theta}$	Material change rate of potential temperature ($\equiv \frac{d\theta}{dt}$), indicating the magnitude of diabatic heating, Equation (6)	$K \cdot s^{-1}$
$\boldsymbol{F}$	Frictional force	$m \cdot s^{-2}$
$\dot{\theta}_h$	Material change rate of potential temperature relating to horizontal gradient of potential temperature and horizontal wind, Equation (6)	$K \cdot s^{-1}$
$\dot{\theta}_v$	Material change rate of potential temperature relating to vertical gradient of potential temperature and vertical motion, Equation (6)	$K \cdot s^{-1}$
$\hbar$	Vertical coordinate in hybrid sigma-pressure system	N/A

(Continues)

T A B L E 1   (Continued)

Symbols and abbreviations	Physical meaning	Unit
$\overline{W}$	Reynolds average of PVD: Obtained by calculating W at each time step using six-hourly data, followed by averaging to monthly mean	$K \cdot m^{-1} \cdot s^{-1}$
$\widetilde{W}$	Slowly varying component of PVD: Directly calculated using monthly mean p, T, and V	$K \cdot m^{-1} \cdot s^{-1}$
W^*	Rapidly varying component of PVD ($\equiv \overline{W} - \widetilde{W}$) that represents the contribution of transient eddy to Reynolds average	$K \cdot m^{-1} \cdot s^{-1}$
$\widetilde{\omega}$	Slowly varying component of ω: Directly calculated using monthly mean V and p	s^{-1}
$\widetilde{\theta}$	Slowly varying component of θ: Directly calculated using monthly mean T and p	K
$\overline{\dot{\theta}_v}$	Reynolds average of $\dot{\theta}_v$	$K \cdot s^{-1}$
$\widehat{\dot{\theta}_v}^{hh}$	Climatological diurnal cycle of $\dot{\theta}_v$ four times daily ($hh \equiv 0000$, 0600, 1200, and 1800 UTC): Directly calculated using Reynolds average of p, T, V, and ω at hh	$K \cdot s^{-1}$
$\overline{\dot{\theta}_v}^{hh}$	Reynolds average of $\dot{\theta}_v$ four times daily	$K \cdot s^{-1}$
[A]	Vertical integral of arbitrary variable A ($\equiv -\int_{p_1}^{p_2} \frac{A}{\rho g} dp$), where p_1 and p_2 indicate the pressure at the bottom and top boundaries, respectively	N/A
p_s	Surface pressure	Pa

2.1 | Reanalysis data

Pressure-level reanalysis data are too coarse in vertical resolution to depict the structure over steep topography and are missing values in low-level isobaric surfaces (Prein and Heymsfield, 2020; Wang *et al.*, 2022). Therefore, terrain-following model-level ERA-interim (ERA-I) reanalysis data in hybrid sigma-pressure coordinates were used to obtain seamless information from the Earth's surface to the upper atmosphere. Owing to the nonlinearity of the PV, six-hourly data were used to depict the contribution of the transient eddies (rapidly varying components relative to the monthly or seasonal mean) to the climatological mean (Reynolds average). For better illustration, the vertical axis of the cross-section figure was donated by the nonuniform increments of pressure at the model level relative to surface pressure, instead of the common pressure coordinate. When the results are shown in figures with a common pressure coordinate, the vertical structure in the lower atmosphere over the TP cannot be well presented because missing values occupied a large vertical extent over the topography. Consequently, the presentation of the information over the TP topography is much poorer than that in the no-topography regions.

Sixty-level, model-level ERA-I reanalysis data from 1979 to 2018 were used. A horizontal gridded output of $2.5° \times 2.5°$ latitude and longitude was used, whereas the original model used to produce the ERA-I data had an approximately 0.75° grid (Dee *et al.*, 2011). All results were obtained from six-hourly data owing to the nonlinearity of the PV. To obtain seamless information from the Earth's surface to the upper atmosphere, over the steep topography, terrain-following model-level data were used instead of pressure-level data. In addition, the monthly mean diabatic heating data from the NCEP-2 reanalysis were used to examine the physical processes. Based on its physical meaning, the NCEP-2 diabatic heating was separated into six components: solar radiative heating, longwave radiative heating, shallow convective heating, deep convective heating, large-scale condensation heating, and vertical diffusive heating. The NCEP-2 data are in a global T62 Gaussian grid on 28 vertical sigma levels and are available for the period 1979–2014 (Kanamitsu *et al.*, 2002).

2.2 | Potential vorticity

We examined the Ertel PV (Ertel, 1942) rather than the quasi-geostrophic PV (Charney and Stern, 1962) because Ertel PV is more accurate. Hereafter, PV refers to the Ertel PV, which is expressed as

$$P = \frac{\boldsymbol{\omega} \cdot \boldsymbol{\nabla}\theta}{\rho} \tag{1}$$

where the three-dimensional absolute vorticity $\boldsymbol{\omega} = 2\boldsymbol{\Omega} + \boldsymbol{\nabla} \times \boldsymbol{U}$, and the three-dimensional gradient operator $\boldsymbol{\nabla} \equiv (\partial_x, \partial_y, \partial_z)$. Density-weighted PV is referred to

as PV density (PVD, Schneider *et al.*, 2003; Wu *et al.*, 2020),

$$W = \rho P = \boldsymbol{\omega} \cdot \boldsymbol{\nabla}\theta \simeq \underbrace{-\partial_z v \partial_x \theta + \partial_z u \partial_y \theta}_{W_h} + \underbrace{(f + \zeta)\partial_z \theta}_{W_v} \quad (2)$$

An alternative term for PV density is PV substance used by Haynes and McIntyre (1990). $\partial_x w$ and $\partial_y w$ were neglected because of their minimal magnitudes. Since we examined the density-weighted PV budget (Section 2.3), we presented the results of PVD instead of PV throughout this study (Schneider *et al.*, 2003; Egger *et al.*, 2015). W_h is the component of PVD that is related to the horizontal potential temperature gradient and horizontal vorticity, whereas W_v is the component of PVD that is related to the static stability and vertical vorticity. In practice, PVD is widely approximated as W_v because W_h is generally much smaller than W_v. However, as elaborated in Section 3.1, W_h was not neglected in this study to achieve the best precision.

Hydrostatic approximation ($\partial_z p = -\rho g$) was used to calculate the vertical gradient referring to z, via a vertical gradient referring to p, using model-level data. Under the geostrophic and hydrostatic approximations in isobaric coordinates, W_h can be expressed as follows:

$$W_h \big|_{\substack{u=u_g \\ v=v_g}} = -\partial_z v_g \partial_x \theta + \partial_z u_g \partial_y \theta = -g f^{-1} \theta^{-1} |\boldsymbol{\nabla}_h \theta|^2 \quad (3)$$

where operator $|\,|$ indicates the norm of the vector. Therefore, W_h is negative under the geostrophic and hydrostatic approximations (Wu and Liu, 1997).

2.3 | PV budget

The PV budget was determined using the PV tendency equation. To view the material change or transport of arbitrary physical variables as Eulerian, conventionally, the PV tendency equation is weighted with density. The PV tendency equation can be formulated for model-level data as follows (Haynes and McIntyre, 1987; Schneider *et al.*, 2003; Egger *et al.*, 2015):

$$\underbrace{\partial_t W}_{\text{TEND}} = \underbrace{-\boldsymbol{\nabla}_h \cdot (W\boldsymbol{V})}_{\text{ADVE}} \underbrace{-\partial_p \cdot (W\omega_{ml})}_{\text{CONV}} + \underbrace{\boldsymbol{\nabla} \cdot (\dot{\theta}\boldsymbol{\omega})}_{\text{DIAB}} + \underbrace{\boldsymbol{\nabla} \cdot (\theta \cdot \boldsymbol{\nabla} \times \boldsymbol{F})}_{\text{FRIC}}$$

$$(4)$$

$$\omega_{ml} = \omega - \partial_t p - u\partial_x p - v\partial_y p \quad (5)$$

$$\dot{\theta} = \partial_t \theta + \boldsymbol{V} \cdot \boldsymbol{\nabla}_h \theta + \underbrace{\omega_{ml} \partial_p \theta}_{\dot{\theta}_v} \quad (6)$$

The left-hand term indicates the local tendency of PV (TEND), while the four right-hand terms indicate the PV tendency induced by advection (ADVE), convection (CONV), diabatic heating (DIAB), and friction (FRIC), respectively. Vertical velocity ω_{ml} was derived from the vertical coordinate transformation rules (Sheng *et al.*, 2021; Xie *et al.*, 2022). $\dot{\theta}$ is the material change rate of potential temperature, which indicates the diabatic heating of the atmosphere. Equations (4) to (6) are more universal than their forms in isobaric coordinates, as ω_{ml} degenerates to ω when $\partial_t p$, $\partial_x p$, and $\partial_y p$ vanish. The deductions are as follows: (i) $\dot{\theta} = \partial_t \theta + \boldsymbol{V} \cdot \boldsymbol{\nabla}_h \theta + \dot{h}\,\partial_h \theta$ for hybrid sigma-pressure coordinates (x, y, h, t); (ii) the original vertical velocity provided in the model-level data is $\omega = \dot{p} = \partial_t p + \boldsymbol{V} \cdot \boldsymbol{\nabla}_h p + \dot{h}\,\partial_h p$; (iii) $\dot{h} = (\omega - \partial_t p - \boldsymbol{V} \cdot \boldsymbol{\nabla}_h p)/\partial_h p$; and (iv) introducing $\dot{h}$ into $\dot{\theta} = \partial_t \theta + \boldsymbol{V} \cdot \boldsymbol{\nabla}_h \theta + \dot{h}\,\partial_h \theta$, we obtain Equations (5) and (6). The deductions for Equation (4) are similar. $\dot{\theta}_h$ is the component of diabatic heating that is related to the horizontal gradient of potential temperature and horizontal wind, whereas $\dot{\theta}_v$ is the component of diabatic heating that is related to static stability and vertical motion (Rodwell and Hoskins, 1996).

The frictional term is estimated as a residual, according to Equation (4), because no reliable method is valid for calculating friction from the reanalysis data. Consequently, the frictional term inherently includes the gravity wave drag effect (Koshyk and McFarlane, 1996). The great density of vertical levels near the surface over the topography could numerically cause an artificially stronger vertical gradient of variables (e.g., $\partial_z \theta$ and $\partial_z \dot{\theta}$) than the flat surface. To avoid this problem, the two boundary model levels were adjusted while calculating the vertical gradient, using finite difference. This adjustment ensured that the pressure interval in calculating the vertical gradient in each grid was the closest to the global mean pressure interval for each vertical level.

2.4 | Transient eddy, frequency filtering, and climatological diurnal cycle

The contribution of the high-frequency (higher than monthly) transient eddy to the climatological mean value of the nonlinear variable was quantified in three ways: transient eddy decomposition, frequency filtering, and climatological diurnal cycle. Following the Reynolds averaging scheme (e.g., Section 3.3.1.2 in Holton (2004)), the transient eddy decomposition of the PVD is:

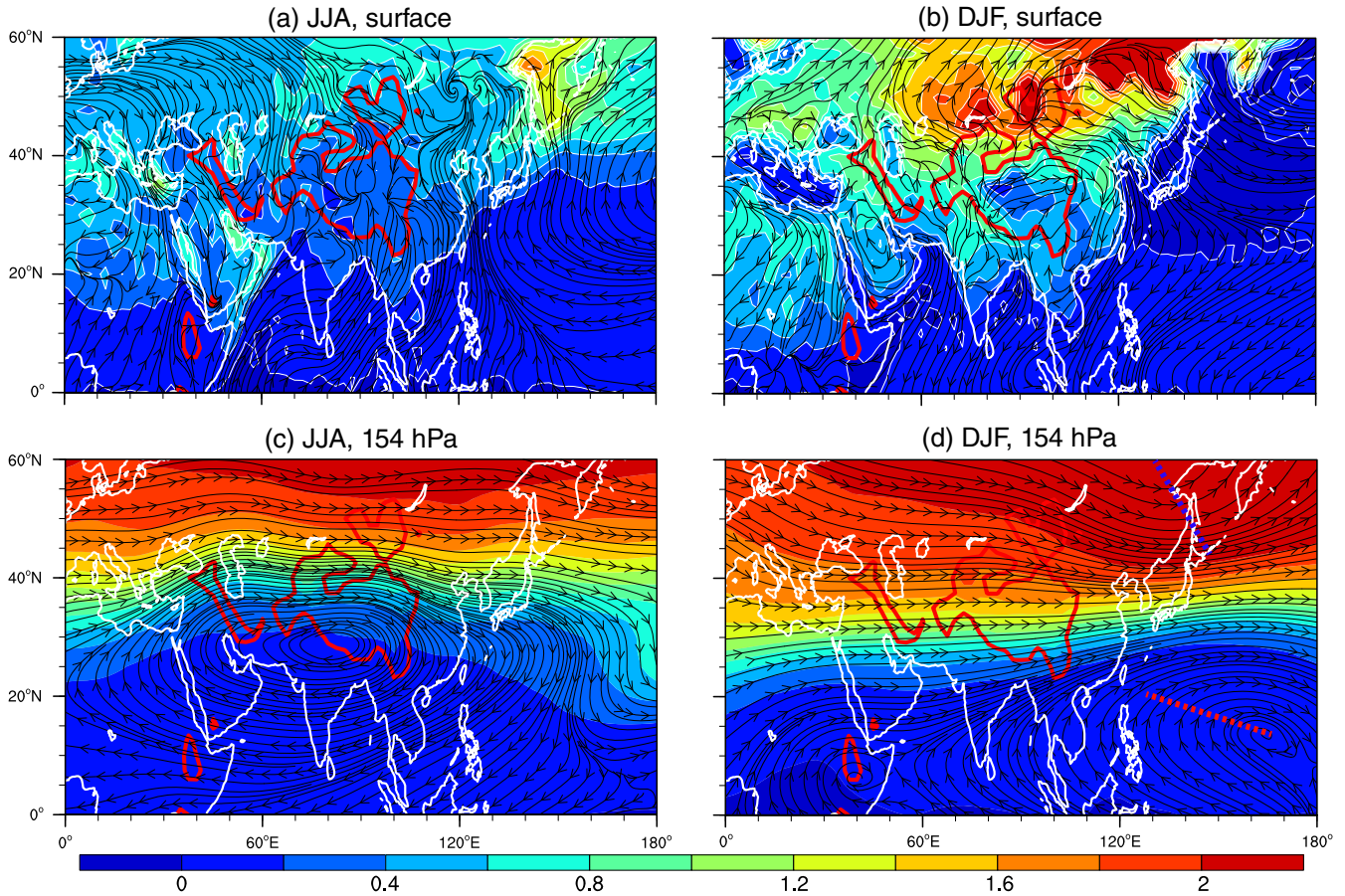## Climatology of PVD (10⁻⁶ k·m⁻¹·s⁻¹) & streamline

FIGURE 1 Climatological mean (1979–2017) PVD (shading) and streamline (black) at the earth surface (lowest model level, No. 60) in (a) JJA and (b) DJF. (c, d) same as (a, b) but at the 28th model level (marked by the red arrow in Figure 2), with a global annual mean pressure of 154 hPa (Figure S1). The red and blue dashed lines indicate the trough and ridge lines of the high and low PVD, respectively. The red contour indicates 1.5 km elevation [Colour figure can be viewed at wileyonlinelibrary.com]

$$\begin{cases} \overline{W} = \overline{\boldsymbol{\omega} \cdot \boldsymbol{\nabla}\theta} = \widetilde{W} + W^* \\ \widetilde{W} = \widetilde{\boldsymbol{\omega}} \cdot \boldsymbol{\nabla}\widetilde{\theta} \\ W^* = \overline{W} - \widetilde{W} \end{cases} \quad (7)$$

where $\overline{W}$ indicates the Reynolds average of W and $\widetilde{W}$ indicates the slowly varying (low-frequency) component of W, calculated using the Reynolds average of p, T, $\boldsymbol{V}$, and ω (Table 1). The contributions of the high-frequency transient eddy to the Reynolds average of the PV budget terms (Equation (4)) and diabatic heating (Equation (6)) were calculated in the same manner.

Frequency filtering is based on Lanczos filtering (Duchon, 1979), which is used to quantify the contributions of transient eddies in the three frequency bands to the monthly mean $\dot{\theta}_v$. The procedures were as follows: (i) p, T, $\boldsymbol{V}$, and ω were filtered into three frequency bands: ultrahigh (1/4–2 days), synoptic (2–12 days), and low (12–30 days); (ii) three components

of $\dot{\theta}_v$ were calculated using variables after filtering, as follows:

$$\overline{\dot{\theta}_v} = \overset{1/4-2}{\overline{\omega_{ml}\partial_p\theta}} + \overset{2-12}{\overline{\omega_{ml}\partial_p\theta}} + \overset{12-30}{\overline{\omega_{ml}\partial_p\theta}} + Residual \quad (8)$$

where $\overset{f_1-f_2}{\overline{\omega_{ml}\partial_p\theta}}$ indicates that the component of $\omega_{ml}\partial_p\theta$ is calculated using p, T, $\boldsymbol{V}$, and ω in the frequency band from f_1 to f_2.

The climatological diurnal cycle ($\widehat{\dot{\theta}_v}^{hh}$) represents the contribution of the Reynolds average of variables ($\overline{p}^{hh}$, $\overline{T}^{hh}$, $\overline{\boldsymbol{V}}^{hh}$, and $\overline{\omega}^{hh}$) to the Reynolds average of $\dot{\theta}_v$ four times daily ($\overline{\dot{\theta}_v}^{hh}$), as follows:

$$\begin{cases} \widehat{\dot{\theta}_v}^{hh} = \widehat{\omega_{ml}}^{hh}\widehat{\partial_p\theta}^{hh} \\ \overline{\dot{\theta}_v}^{hh} = \overline{\omega_{ml}\partial_p\theta}^{hh} \end{cases}, \quad hh \equiv 0000, 0600, 1200, \text{ and } 1800 \text{ UTC} \quad (9)$$

In addition to the climatological diurnal cycle $\widehat{\theta}_v^{hh}$, $\overline{\theta}_v^{hh}$ includes the contribution of additional transient eddies.

2.5 | Radiosonde data over the TP

Radiosonde observations, obtained during the Third Tibetan Plateau Atmospheric Experiment (Zhao et al., 2017), were used to verify the climatological diurnal cycle of the vertical profile of the potential temperature over the TP. Observations were made at five sites during the summer of 2014. Three variables (temperature, pressure, and altitude) from the radiosonde measurements were used to calculate the vertical gradient of the potential temperature.

3 | RESULTS

3.1 | Climatology of PV over the TP

Planetary vorticity (f, Equation (2)) constrained the background of the increasing PVD with latitude (Figure 1). The near-surface PVD over land was larger than that over the ocean (Figure 1a, b). Because the atmospheric circulation over the ocean was generally stronger than that over land, the land-sea differences in near-surface PVD must be dominated by thermodynamic factors, that is, static stability $\partial_z\theta$. Static stability was also responsible for the stronger near-surface PVD over land in winter than in summer because the low near-surface potential temperature due to the cold land surface in winter enhanced $\partial_z\theta$ and W_v (a component of PVD due to the static stability and vertical vorticity, Equation (2)).

In the upper troposphere, a low PVD ridge over the TP was prominent in summer (Figure 1c), which corresponds to the Asian monsoon anticyclone (Hoskins, 1991). This low PVD ridge has been suggested to be influenced by diabatic heating of the TP (Wu et al., 2015a, 2016; Liu et al., 2017). In contrast, a study by Boos and Kuang (2010) suggested a limited influence of TP heating. However, problems in experimental design and theoretical interpretation indicate that Boos and Kuang (2010) likely underestimated the influence of TP heating: first, the experiment design of Boos and Kuang (2010) factored the influence of the TP heating below 600 hPa into the mechanical influence of the TP (Wu et al., 2012); second, the upper-troposphere temperature maximum coinciding with the low PVD ridge is determined by the large-scale zonal distribution of vertical gradient of diabatic heating (Wu et al., 2015a), rather than the local vertical coupling in the statistical-equilibrium theory as suggested by Boos and Kuang (2010). In winter, a high PVD trough around
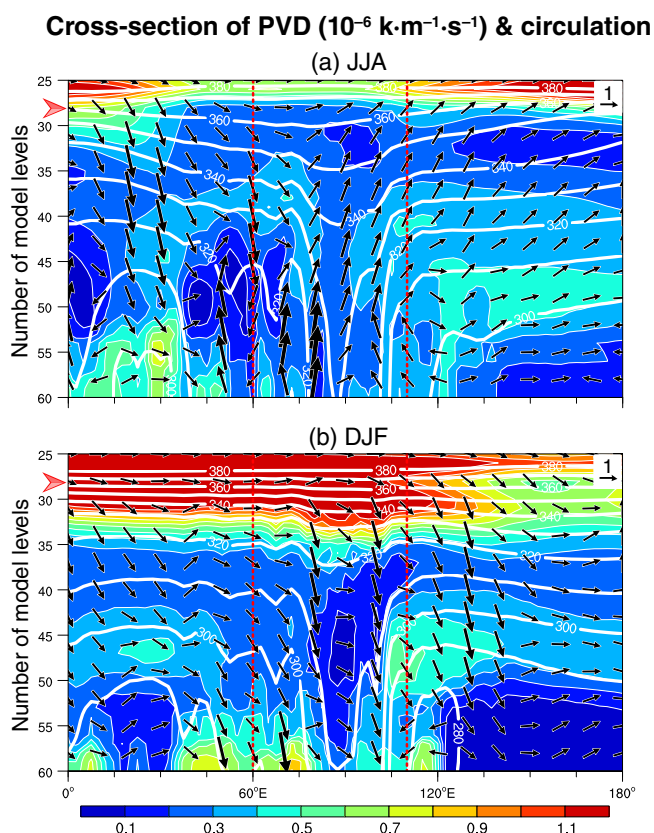
Cross-section of PVD (10⁻⁶ k·m⁻¹·s⁻¹) & circulation

FIGURE 2 Vertical-latitudinal cross-section (averaged over 30°–35° N) of the climatological mean PVD and circulation (u, $-\omega \times 20$) in (a) JJA and (b) DJF; u and v are in units of m · s⁻¹ and ω is in units of Pa · s⁻¹. The white contour indicates the isentrope. The vertical axis indicates the number of model levels, wherein the red arrow marks the 28th model level. The red dashed lines mark the location of the TP [Colour figure can be viewed at wileyonlinelibrary.com]

140° E was associated with the East Asian deep trough and a low PVD ridge around 145° E in the south was associated with a subtropical high (Figure 1d). The 28th model level was chosen to represent the upper troposphere because it has a global annual mean pressure of 154 hPa (Figure S1), which is close to the target pressure level of 150 hPa. The conclusions were not influenced when selecting other adjacent model levels (not shown).

The cross-sections (Figure 2) further demonstrated the three-dimensional configurations between PVD and circulation. The distributions of PVD in the middle and low troposphere over the TP were similar in summer and winter (Figure 2), whereas the distributions of PVD in the upper troposphere were seasonally different. Specifically, the PVD in the middle and low troposphere over the TP platform (approximately 90° E) was lower than that over the surrounding areas (Figure 2), whereas the low (high) PVD in the upper troposphere was over the TP in JJA (DJF) and accompanied by an ascending (sinking) motion.

Climatology of W_h (10^{-6} k·m^{-1}·s^{-1})
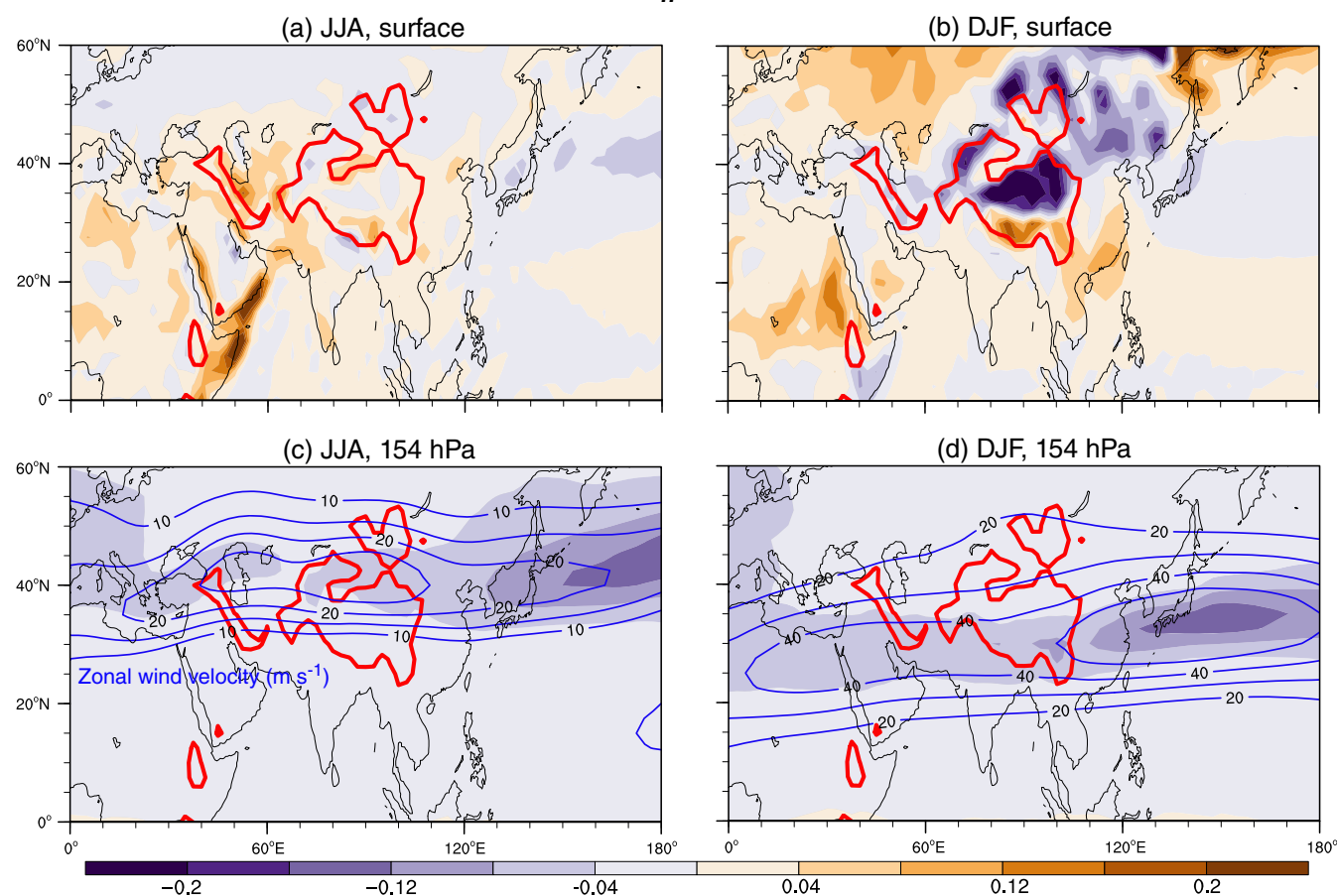

FIGURE 3   Climatological mean W_h (Equation (2)) at the earth surface (lowest model level, No. 60) in (a) JJA and (b) DJF. (c, d) Same as (a, b) but at the 28th model level, with a global annual mean pressure of 154 hPa. The blue contour indicates the zonal wind velocity. The red contour indicates 1.5 km elevation [Colour figure can be viewed at wileyonlinelibrary.com]

The distributions of PVD over the Rocky Mountains (approximately 110° W) were similar but weaker and smaller in magnitude and scale (Figure S2).

The lower PVD over the TP platform (approximately 90° E) than that over the surroundings (Figure 2) was determined by the weaker static stability (Figure S3), which was set by a high near-surface potential temperature owing to low pressure. In contrast to the overall weakened static stability in response to a high potential temperature anomaly over a flat surface (figure 16a in Hoskins *et al.* (1985)), the static stability and PVD over the periphery of the TP were enhanced (Figure 2). This indicates a difference between the heating on sloped and flat surfaces. In addition to numerical simulations (Wu *et al.*, 2016), the effects of diabatic heating on three-dimensional circulation and PV configuration over the TP remain unclear. These problems were unpacked through a comprehensive PV budget analysis.

The complete form of PVD includes the component due to the horizontal potential temperature gradient and

horizontal vorticity (W_h) and the component due to the static stability and vertical vorticity (W_v). However, only W_v is widely used because W_h is negligible in most cases. Although W_h is much smaller than the W_v, previous studies have shown that W_h is crucial for vortex development and severe weather (Wu and Liu, 1997; Zheng *et al.*, 2013). The W_h near the surface had a large magnitude around regions where the horizontal potential temperature gradient was strong, such as the topography regions (Figures 3a, b and S4). Because W_h was negative under the geostrophic approximation (Equation (3)), both geostrophic (negative) and ageostrophic (positive) motions existed near the surface. In addition, W_h was higher in the upper troposphere along the jet stream than that in other regions (Figure 3c, d). The negative W_h along the jet stream was strongest over the Pacific Ocean. This negative W_h partly (i.e., in a ratio of 1/4 for W_h/W_v as shown in Figure S4) contributed to the upper-tropospheric low PVD downstream TP (approximately 145° E in Figure 2b), which was related to the advective redistribution of PVD, as elaborated on in the next section.
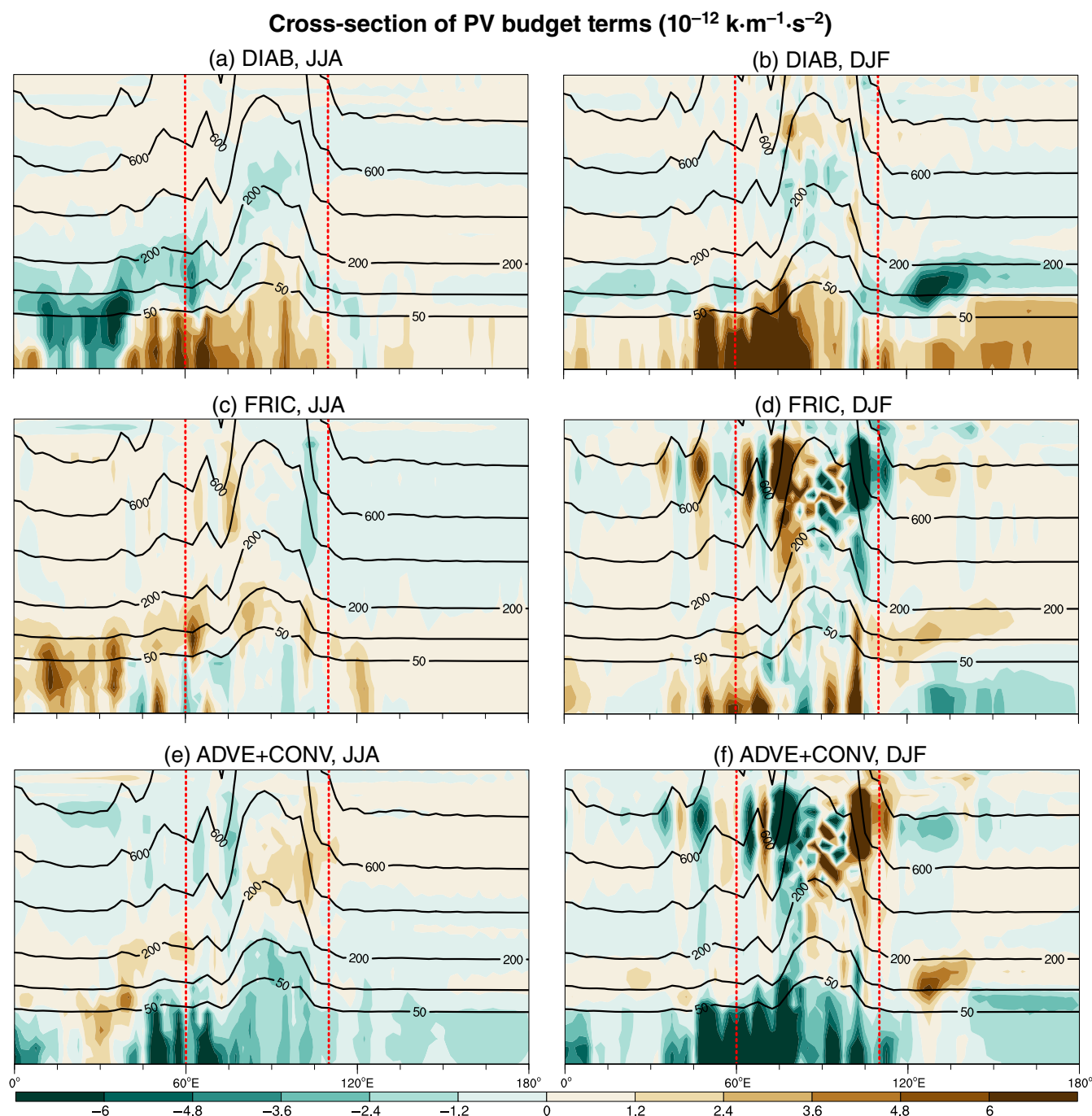
Cross-section of PV budget terms (10^{-12} k·m^{-1}·s^{-2})

FIGURE 4 Vertical-latitudinal cross-section (averaged over 30°–35° N) of the climatological mean of four PV budget terms (Equation (4)): (a) diabatic heating-generated PVD (DIAB); (c) friction-generated PVD (FRIC); and (e) sum of horizontal advective (ADVE) and vertical convective (CONV) redistribution of PVD in JJA. (b, d, f) Same as (a, c, e) but for results in DJF. The black contours indicate the pressure increments relative to surface pressure, which represents the non-uniform vertical axis. The red dashed lines mark the location of the TP [Colour figure can be viewed at wileyonlinelibrary.com]

3.2 | Balanced PV budget over the TP

The PV budget was examined to understand the PV climatology over the TP. Diabatic heating-generated PVD tendency within the boundary layer (approximately within a 50 hPa extent above the surface) was positive

over the TP and Iranian (approximately 50° E) Plateaus in summer and winter (Figure 4a, b). Owing to the small magnitude of the frictional term, the near-surface PV budget balance in summer, was mainly between the positive diabatic term and negative advective/convective term (Figure 4a, c, e). In contrast, the frictional term was not

Cross-section of $\partial_z\dot\theta$ (10^{-8} k·m^{-1}·s^{-1})
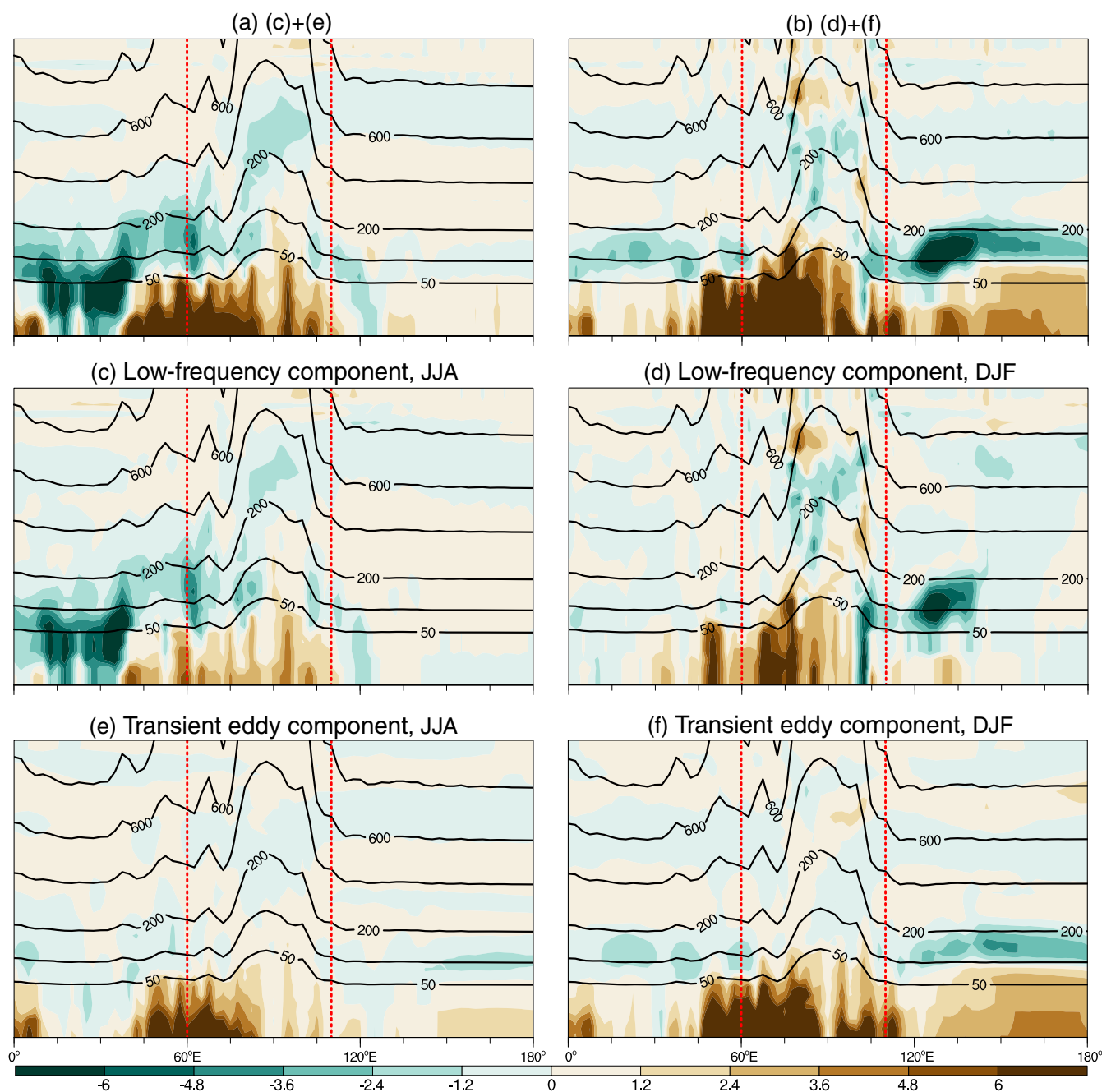

FIGURE 5 Vertical-latitudinal cross-section (averaged over 30°–35° N) of the vertical gradient of diabatic heating ($\partial_z\dot\theta$) in (a) JJA and (b) DJF. (c, d) and (e, f) Same as (a, b) but for the low-frequency component and high-frequency transient eddy component (Section 2.4), respectively. The black contours indicate the pressure increments relative to surface pressure, which represents the non-uniform vertical axis. The red dashed lines mark the location of the TP [Colour figure can be viewed at wileyonlinelibrary.com]

negligible in winter; therefore, the near-surface PV budget balance was among all three terms (Figure 4b, d, f).

The diabatic heating-generated positive PVD tendency within the boundary layer in summer and winter (Figure 4a, b) favoured a near-surface high PVD over the TP (Figure 2). The friction-generated positive PVD tendency in winter (Figure 4d) had a secondary contribution

to the near-surface high PVD over the TP. Consequently, the higher near-surface PVD in winter than in summer was caused by stronger PV generation by diabatic heating and friction in winter (Figure 4a–d).

The diabatic heating-generated PVD tendency (Figure 4a, b) was dominated by the vertical gradient of diabatic heating ($f\partial_z\dot\theta$; Figure 5a, b), whereas the
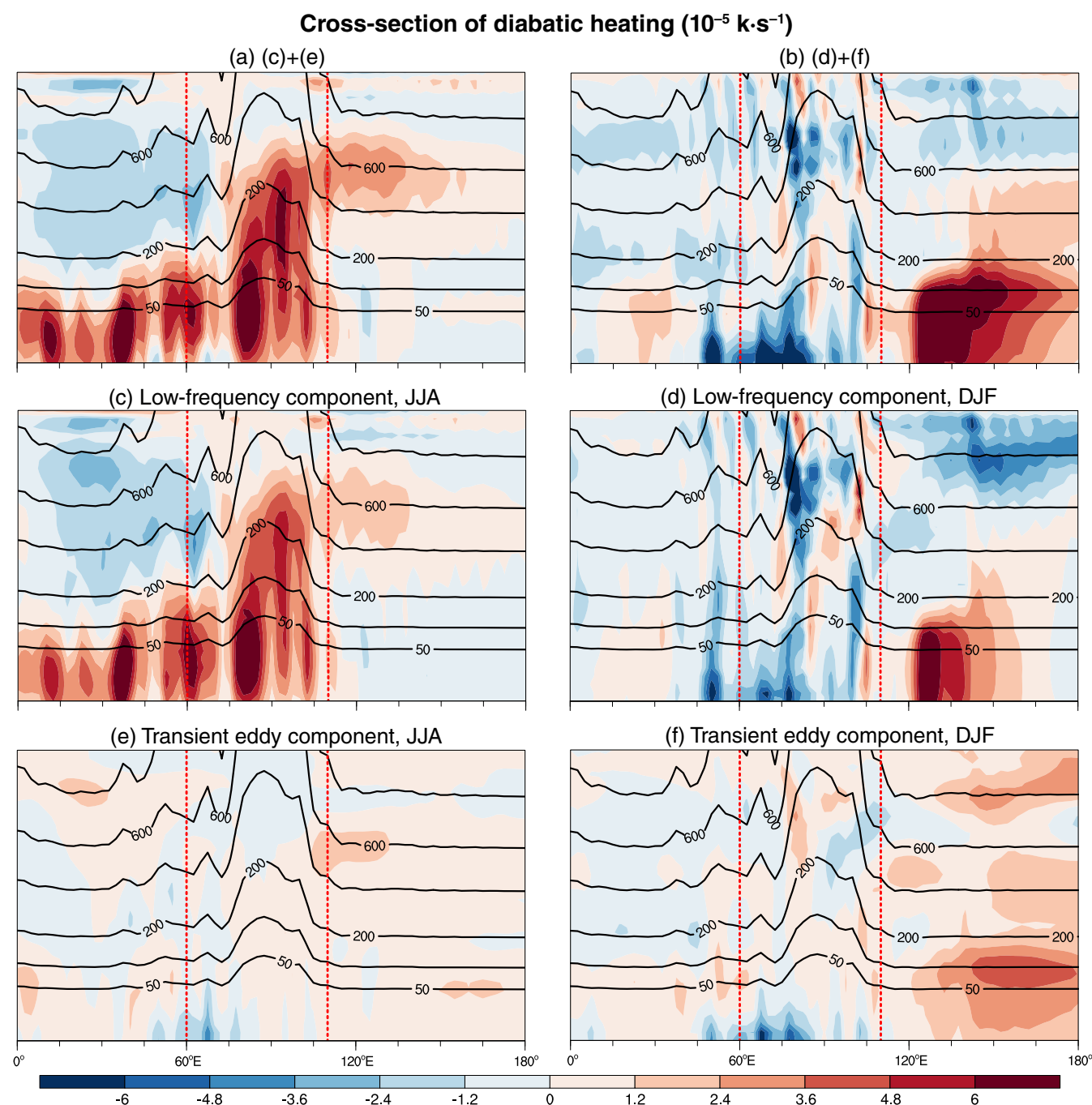
Cross-section of diabatic heating (10⁻⁵ k·s⁻¹)

FIGURE 6 Same as Figure 5 but for diabatic heating, $\dot{\theta}$ [Colour figure can be viewed at wileyonlinelibrary.com]

contributions of the horizontal gradient of diabatic heating and the relative vorticity ζ are negligible. Therefore, diabatic heating-generated near-surface positive PVD tendency over the TP was determined by increasing diabatic heating with height in summer and winter. Nonetheless, diabatic heating was positive in summer and negative in winter (Figure 6a, b); that is, TP was a heat source and sink in summer and winter, respectively (Wu *et al.*, 2007).

The high-frequency transient eddy component contributed more to the diabatic heating-generated positive

PVD tendency within the boundary layer than that of the low-frequency component (Figure 5c–f), wherein $\partial_z \dot{\theta}_v$ was dominant than $\partial_z \dot{\theta}_h$ (Equation (6); Figure S5). Importantly, the relative magnitudes of $\partial_z \dot{\theta}$ between high- and low-frequency components (Figure 5c–f) were the opposite to that of $\dot{\theta}$; namely, the high-frequency component of diabatic heating was smaller than that of the low-frequency component (Figure 6). Therefore, although the high-frequency component of diabatic heating is smaller in magnitudes than the low-frequency
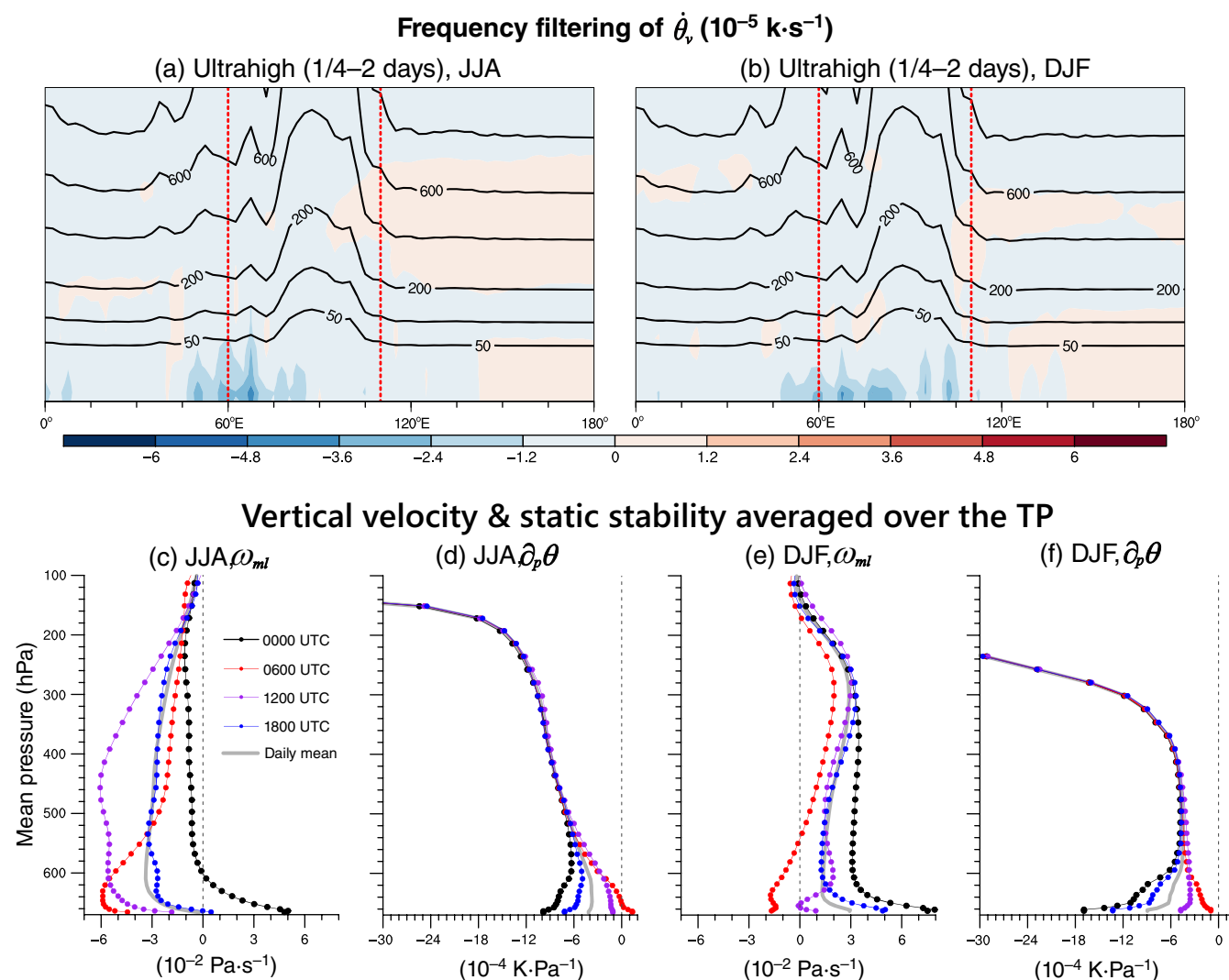
Frequency filtering of $\dot{\theta}_v$ (10^{-5} k·s^{-1})

Vertical velocity & static stability averaged over the TP

FIGURE 7 Vertical-latitudinal cross-section (averaged over 30°–35°N) of the climatological mean of the frequency filtered $\dot{\theta}_v$ (ultrahigh 1/4–2 days, equation (8)) in (a) JJA and (b) DJF. The black contours indicate the pressure increments relative to surface pressure, which represents the non-uniform vertical axis. The red dashed lines mark the location of the TP. (c) Climatological diurnal cycle (Equation (9)) of the regional mean (c, e) vertical velocity ω_{ml} and (d, f) static stability $\partial_p\theta$ averaged over the TP (20°–40° N, 60°–110° E, higher than 1.5 km) at 0000, 0600, 1200, 1800 UTC in (c, d) JJA and (e, f) DJF, respectively. The vertical axis indicates the regional mean pressure. The results for the other frequency band and the climatological diurnal cycle of $\dot{\theta}_v$ and $\partial_z\dot{\theta}_v$ are shown in Figure S6 [Colour figure can be viewed at wileyonlinelibrary.com]

component, the high-frequency transient eddy component of $\dot{\theta}_v$ is crucial in shaping $\partial_z\dot{\theta}$ within the boundary layer.

Frequency filtering demonstrated that the ultrahigh-frequency component (1/4–2 days; Section 2.4) was dominant for the high-frequency component of $\dot{\theta}_v$ within the boundary layer (Figures 7a, b and S6). Stimulated by the diurnal cycle-induced boundary layer wind maximum (Blackadar, 1957), further investigations demonstrated that the climatological diurnal cycle (Section 2.4; Figure 7c–f) dominated the negative ultrahigh-frequency component of $\dot{\theta}_v$ (Figures 7a, b and S6) within the boundary layer. $\dot{\theta}_v = \omega_{ml}\partial_p\theta < 0$ includes two cases: case I is

$\omega_{ml} > 0$ (sinking) and $\partial_p\theta < 0$ (static stable); case II is $\omega_{ml} < 0$ (ascending) and $\partial_p\theta > 0$ (static unstable). In summer (Figure 7c, d), case I (0000 UTC) contributed more to negative $\dot{\theta}_v$ than case II (0600 UTC). In winter (Figure 7e, f), case I (0000, 1200, and 1800 UTC) led to negative $\dot{\theta}_v$ because case II did not appear at 0600 UTC. The diurnal cycle of the vertical gradient of the potential temperature in summer was confirmed by the radiosonde observations shown in Figure S7; namely, strong stable stratification at 0000 and 1800 UTC, weak stable stratification at 1200 UTC, and unstable stratification at 0600 UTC within the low boundary layer. In contrast, because the ω_{ml} and $\partial_p\theta$ were diurnally less variant above the

FIGURE 8 Climatology of the regional mean diabatic heating averaged over the TP (20°–40°N, 60°–110°E, higher than 1.5 km) in (a) JJA and (b) DJF based on NCEP-2 data. The vertical axis indicates the regional mean pressure. The six physical components are solar ($\dot{\theta}_{SW}$) and longwave ($\dot{\theta}_{LW}$) radiative, shallow ($\dot{\theta}_{SC}$) and deep ($\dot{\theta}_{DC}$) convective, large-scale condensation ($\dot{\theta}_{LC}$), and vertical diffusive ($\dot{\theta}_{VD}$) heating [Colour figure can be viewed at wileyonlinelibrary.com]

Diabatic heating over the TP

TABLE 2 Regional mean of the vertical integral values of PV budget terms (equation (4)), PVD, relative vorticity $\rho\zeta$, and static stability $\partial_z\theta$, over the TP for three vertical ranges: Below 500, 300–500, and 100–300 hPa. ζ is weighted by density, whereas PVD and PV budget terms are already in density-weighted form. Vertical integral is calculated according to formula $[A] = -\int_{p_1}^{p_2} \frac{A}{\rho g} dp$ (Table 1), where $p_1 = p_s$, 500, 300, and $p_2 = 500, 300, 100$. The bracketed numbers in the PVD column indicate values after removing the zonal mean. Note that the finite difference and vertical integration induce that the PV budgets are not strictly closed

	Vertical integral of PV budget terms (10^{-10} K s^{-2})							
	JJA				**DJF**			
	DIAB	FRIC	CONV	ADVE	DIAB	FRIC	CONV	ADVE
500–p_s	3.8	18.5	−27.3	3.0	37.2	11.9	−33.2	−17.6
300–500	−18.5	7.0	13.0	−1.7	−10.6	7.1	−3.1	6.2
100–300	0	−1.2	−11.2	10.3	32.1	3.8	−40.2	5.7
	Vertical integral of PVD (10^{-3} K s^{-1}), $\rho\zeta$ (10^{-2} kg s^{-1} m^{-2}), and $\partial_z\theta$ (K)							
	JJA			**DJF**				
	PVD	$\rho\zeta$	$\partial_z\theta$	PVD	$\rho\zeta$	$\partial_z\theta$		
500–p_s	0.6 (0)	0.3	8	0.6 (0.1)	0	9		
300–500	1.2 (0.2)	−0.9	17	0.8 (0)	0.9	12		
100–300	2.9 (−1.2)	−3.7	46	7.9 (1.4)	3.1	83		

boundary layer (Figure 7c–f), they corresponded to the low-frequency component; namely positive (heat source) and negative (heat sink) in summer and winter, respectively. Therefore, in addition to the low-frequency component, the climatological diurnal cycle is crucial for the positive diabatic heating-generated PVD tendency within the boundary layer via modifying the vertical structure of diabatic heating.

The impacts of the TP on PV in the middle and upper troposphere in summer were distinct because prominent signatures in the three PV budget terms in summer appeared only over the TP (Figures 4a and S8). The three PV budget terms in the middle and upper troposphere in winter over the TP were also the strongest relative to those over the Rocky Mountains (Figure S8). The mid-tropospheric diabatic

heating-generated PVD tendency over the TP was negative in summer and was mainly balanced by the advective/convective redistribution term (Figure 4a, e), wherein convective redistribution was dominant (Figure S9). The balance in the middle and upper troposphere in winter was between the frictional term and the advective/convective term (Figure 4d, f), wherein advective redistribution was dominant (Figure S9). In addition, gravity wave drag may dominate the frictional term (Koshyk and McFarlane, 1996) because it is strong in the middle and upper troposphere where friction is weak.

Diabatic heating-generated negative PVD tendency in the middle troposphere (Figure 4a), favouring a low PVD over the TP in summer (Figure 2a). The low PVD in the upper troposphere over the Pacific in winter (approximately
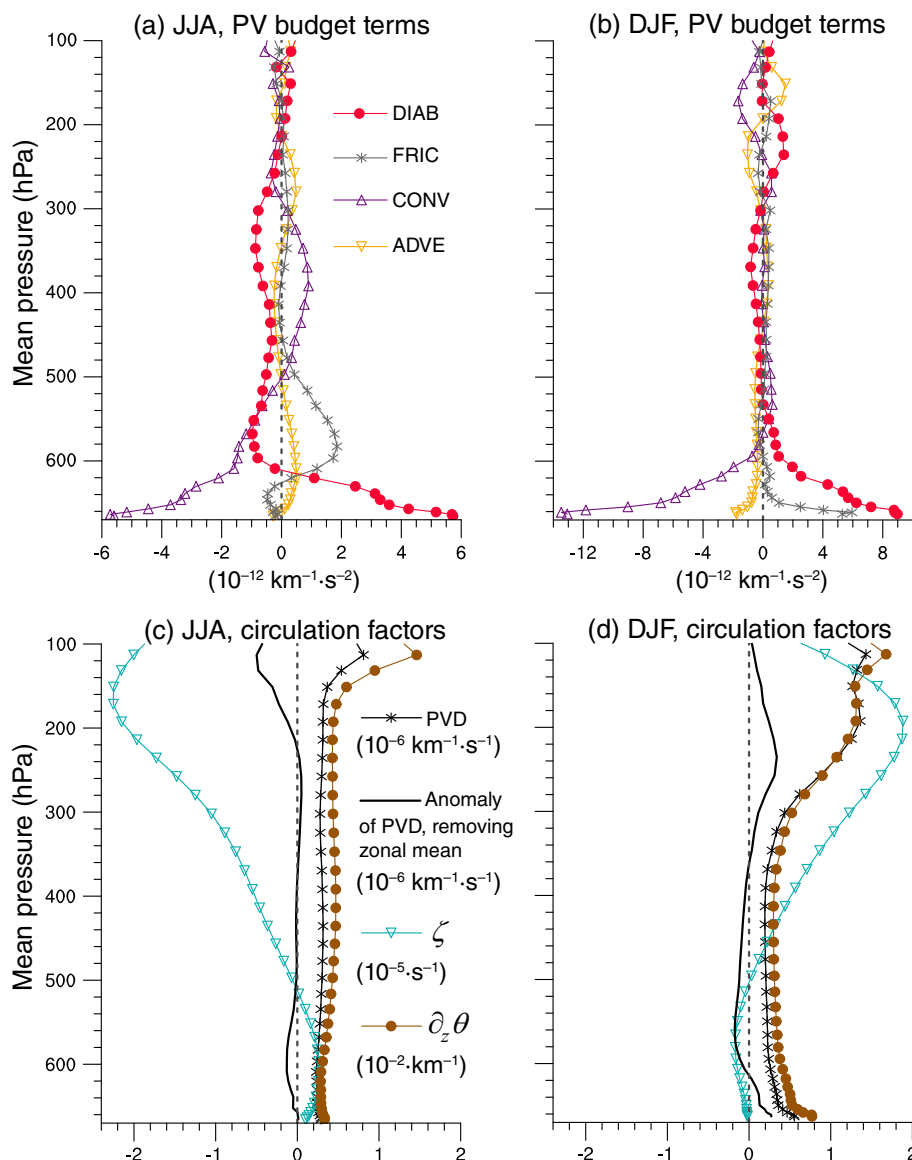
FIGURE 9 Climatology of the four regional mean PV budget terms (Equation (4)), averaged over the TP (20°–40° N, 60°–110° E, higher than 1.5 km), in (a) JJA and (b) DJF. (c, d) Same as (a, b) but for PVD, the anomaly of PVD after removing zonal mean, relative vorticity ζ, and static stability $\partial_z\theta$. The vertical axis indicates the regional mean pressure [Colour figure can be viewed at wileyonlinelibrary.com]

145° E in Figures 1d, 2b, and 3d) was favoured by advective redistribution (Figures 4f and S9) of the friction-generated negative PVD tendency over the eastern TP (Figure 4d). Therefore, PV generation over the TP is crucial for downstream circulation in the Pacific Ocean in winter. In addition, diabatic heating-generated negative PVD tendency in the middle troposphere in summer over the TP (Figure 4a) was induced by decreasing positive diabatic heating with height (Figures 5a and 6a), which was dominated by the low-frequency component (Figure 6c), in contrast to the case within the boundary layer.
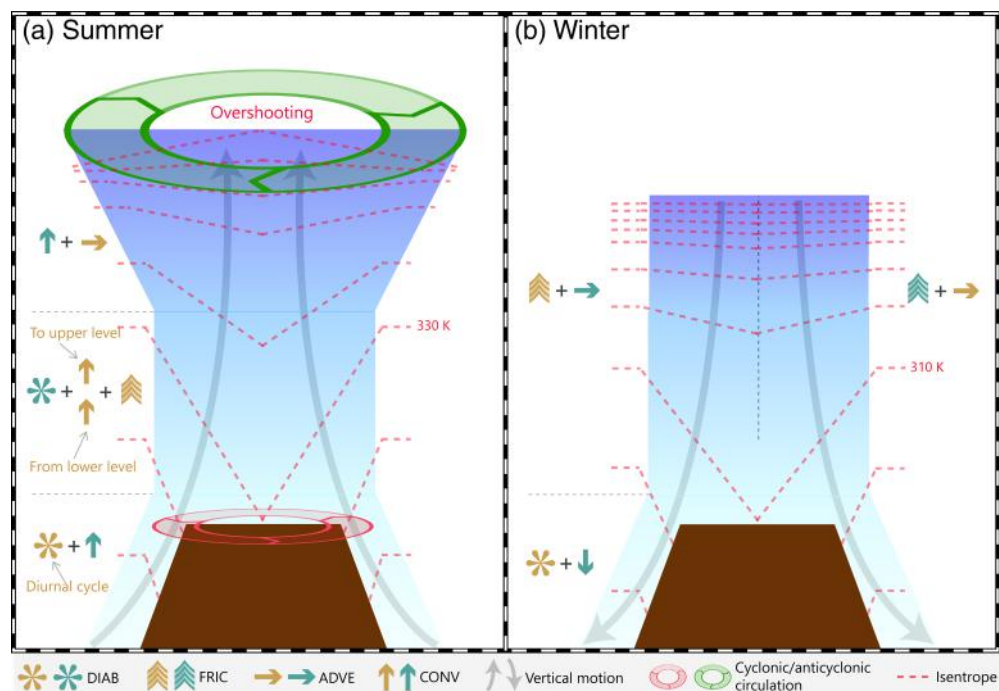
3.3 | PV budget view of the circulation climatology over the TP

The physical processes contributing to total diabatic heating include solar and longwave radiation, shallow and deep convection, large-scale condensation, and vertical diffusion (Figure 8). Among these, longwave cooling, deep convection, and large-scale condensation had diabatic heating profiles that increased with height within the boundary layer, thereby leading to a positive vertical gradient of diabatic heating. In contrast, vertical diffusion (i.e., sensible heating) generated positive diabatic heating that decreased with height in summer, leading to a negative vertical gradient of diabatic heating, while vertical diffusive heating was negative and had a weak positive gradient in winter. Consequently, because of the opposite effects of sensible heating in diabatic PV generation in summer and winter, the diabatic heating-generated positive PVD tendency was stronger in winter than in summer.

In addition, the two cases of the diurnal cycle were related to these physical processes. Specifically, warming due to the sinking motion in case I balanced the longwave cooling, whereas the convection of case II

FIGURE 10 Schematic PV budget view of the circulation climatology over the TP in (a) summer and (b) winter. The first four symbols in brown and turquoise colours at the bottom indicate the four PV budget terms (Equation (4)) with positive and negative values, respectively. The last three symbols at the bottom indicate vertical motion, cyclonic/anticyclonic circulation, and isentrope, respectively. The brown trapezoid and gradient blue shading indicate the TP topography and atmosphere aloft, respectively [Colour figure can be viewed at wileyonlinelibrary.com]

transported the near-surface heat induced by strong solar heating upward during the daytime. The magnitudes of the diabatic heating-generated PVD tendency associated with the climatological diurnal cycle were also stronger in winter than in summer (Figures 7 and S6). Therefore, the opposite sensible heating (i.e., heating source and sink in summer and winter, respectively) and different magnitudes of contribution from the climatological diurnal cycle jointly induced a stronger diabatic heating-generated PVD tendency in winter than in summer.

The piecewise vertical integral of the PV budget terms and dynamic (vorticity) and thermodynamic (static stability) circulation factors were further examined (Table 2 and Figure 9). In summer, diabatic heating-generated positive PVD stimulates cyclonic circulation development near the surface over the TP (Table 2 and Figure 9a, c). Ascending motion transported the diabatic heating- and friction-generated positive PVD upward to the middle troposphere so that the balanced PVD in the low troposphere (below 500 hPa) over the TP was close to the zonal mean (Table 2 and Figure 9a, c). In contrast, diabatic heating-generated negative PVD tendency stimulated anticyclonic circulation in the middle troposphere (300–500 hPa), wherein this negative PVD tendency was jointly balanced by the positive PVD input from the low troposphere, upward transportation of the low PVD to the upper troposphere, and frictional dissipation (Table 2 and Figure 9a, c). The balance between the convective and advective redistribution of PVD was prominent in the upper troposphere (100–300 hPa) where diabatic heating was weak. Particularly, a low PVD input from the middle troposphere induced a

low PVD in the upper troposphere over the TP (Table 2 and Figure 9a, c), wherein horizontal advection further spreads the vertically inputted low PVD to a larger scope, pertaining to the Asian monsoon anticyclone. The extended influence of mid-tropospheric diabatic heating on upper-tropospheric PVD was referred to as overshooting by Wu and Liu (2000), who addressed the PV budget of ideal vertically symmetric convective heating (Supplementary text).

In winter, diabatic heating generated a positive PVD near the surface (Figure 9b), like that in summer (Figure 9a). However, the dynamic processes differ between summer and winter. Particularly, the near-surface negative PVD tendency due to convective redistribution (Figure 9b) was induced by downward low PVD input through a sinking motion in winter (Figure 2b). The joint effects of diabatic heating- and friction-generated positive PVD tendency and negative PVD tendency due to convective redistribution make the PVD and ζ in the low troposphere over the TP close to the zonal mean (Table 2 and Figure 9b, d). For the middle to upper troposphere, the balanced frictional term and advective/convective redistribution term of the PV budget have a dipole pattern whose average is meaningless. Therefore, a balanced PV budget due to gravity wave drag and advective redistribution is crucial in winter (Figure 4); specifically, gravity wave drag-generated negative PVD tendency over the eastern TP and its downstream advection are crucial for circulation in the Pacific. A PV budget view of the circulation climatology over the TP during summer and winter is shown schematically in Figure 10.

4 | DISCUSSION AND CONCLUSIONS

Although previous studies partly examined PV over the TP (Wu *et al.*, 2016), this study provided a more comprehensive three-dimensional PV budget for circulation over the TP, in both summer and winter. Consequently, this study demonstrated the dynamic mechanisms in the formation of circulation climatology over the TP from a PV budget perspective, as schematically shown in Figure 10. Our results provide new insights into the formation of near-surface cyclonic circulation, coupled with upper-tropospheric low PV and anticyclonic circulation, in summer and the effect of gravity wave drag and its downstream influence via advective redistribution of PV in winter. In particular, the crucial role of the diurnal cycle in shaping the climatological near-surface cyclonic circulation in summer was demonstrated. Although previous studies suggested an obvious diurnal cycle in the PV itself, near the surface over the TP (Ma *et al.*, 2020; Sheng *et al.*, 2021), the contribution of the diurnal cycle to the climatological mean PV budget has not yet been examined. In addition, PV budget analysis demonstrated the extended influence of mid-tropospheric diabatic heating on the upper-tropospheric low PV associated with the Asian monsoon anticyclone and monsoonal overturning circulation, that is, overshooting mechanism. Since the diabatic heating over the TP favoured the northward extension of the South and East Asian summer monsoons (Wu *et al.*, 2012, 2016), the contribution of the diabatic heating over the TP to the Asian monsoon anticyclone, relative to that of monsoonal diabatic heating, should be further quantified by combining numerical simulations with PV budget analysis.

Further investigations should verify the effect of gravity wave drag in winter, such as via numerical simulation (Koshyk and McFarlane, 1996), because gravity wave drag-induced PVD was estimated as the residual of the PV budget in this study. Additionally, revealing the influence of PV sources present on the Earth's surface on atmospheric circulation is paramount and challenging (Held and Schneider, 1999; Plumb and Ferrari, 2005; Schneider, 2005). The TP topography may be a crucial surface PV source because the isentropic surface intersects the TP. Therefore, in addition to local circulation, the PV budget view can also be used to investigate the dynamics underlying the remote influences of the TP, especially its surface PV source, on weather and climate. In particular, previous studies suggested that the TP influences the climate of upstream Eurasia and Africa via zonal-vertical circulation cells and Rossby waves (Lu *et al.*, 2018; Nan *et al.*, 2019; Liu *et al.*, 2020b) and the climates of the Indian Ocean, downstream Asia, Pacific Ocean, North America, and Atlantic Ocean via Rossby waves and meridional-vertical circulation cells (Wu *et al.*, 2007; Zhao *et al.*, 2007; Park *et al.*, 2013; Sun *et al.*, 2019; Yang *et al.*, 2020; You *et al.*, 2020; Liu *et al.*, 2020a; Lu *et al.*, 2021); tropical cyclones (Baldwin *et al.*, 2019); and weather, including synoptic temperature variability in winter around the TP (Lutsko *et al.*, 2019), Eurasian heatwaves in summer (Wu *et al.*, 2015b), and downstream severe weather in China (Wu *et al.*, 2020; Ma *et al.*, 2022)

ORCID

Guoxiong Wu https://orcid.org/0000-0002-1838-1951

REFERENCES

Adames, Á.F. and Ming, Y. (2018) Interactions between water vapor and potential vorticity in synoptic-scale monsoonal disturbances: moisture vortex instability. *Journal of the Atmospheric Sciences*, 75, 2083–2106.

Amemiya, A. and Sato, K. (2020) Characterizing quasi-biweekly variability of the Asian monsoon anticyclone using potential vorticity and large-scale geopotential height field. *Atmospheric Chemistry and Physics*, 20, 13857–13876.

Attinger, R., Spreitzer, E., Boettcher, M., Wernli, H. and Joos, H. (2021) Systematic assessment of the diabatic processes that modify low-level potential vorticity in extratropical cyclones. *Weather and Climate Dynamics*, 2, 1073–1091.

Baldwin, J.W., Vecchi, G. and Bordoni, S. (2019) The direct and ocean-mediated influence of Asian orography on tropical precipitation and cyclones. *Climate Dynamics*, 53, 805–824.

Blackadar, A.K. (1957) Boundary layer wind maxima and their significance for the growth of nocturnal inversions. *Bulletin of the American Meteorological Society*, 38, 283–290.

Büeler, D. and Pfahl, S. (2017) Potential vorticity diagnostics to quantify effects of latent heating in extratropical cyclones. Part I: methodology. *Journal of the Atmospheric Sciences*, 74, 3567–3590.

Boos, W.R. and Kuang, Z. (2010) Dominant control of the South Asian monsoon by orographic insulation versus plateau heating. *Nature*, 463, 218–222.

Cai, M. (2003) Potential vorticity intrusion index and climate variability of surface temperature. *Geophysical Research Letters*, 30, 1119.

Charney, J.G. and Stern, M. (1962) On the stability of internal baroclinic jets in a rotating atmosphere. *Journal of the Atmospheric Sciences*, 19, 159–172.

Davis, C.A. and Emanuel, K.A. (1991) Potential vorticity diagnostics of cyclogenesis. *Monthly Weather Review*, 119, 1929–1953.

Dee, D., Uppala, S.M., Simmons, A., Berrisford, P., Poli, P., Kobayashi, S., Andrae, U., Balmaseda, M.A., Balsamo, G., Bauer, P., Bechtold, P., Beljaars, A., Van de Berg, L., Bidlot, J., Bormann, N., Delsol, C., Dragani, R., Fuentes, M., Geer, A.J., Haimberger, L., Healy, S.B., Hersbach, H., Holm, E.V., Isaksen, L., Kållberg, P.W., Köhler, M., Matricardi, M., Mcnally, A., Monge-Sanz, B., Morcrette, J.J., Park, B., Peubey, C., de Rosnay, P., Tavolato, C., Thepaut, J. and Vitart, F. (2011) The ERA-Interim reanalysis: configuration and performance of the data assimilation system. *Quarterly Journal of the Royal Meteorological Society*, 137, 553–597.

Duchon, C.E. (1979) Lanczos filtering in one and two dimensions. *Journal of Applied Meteorology and Climatology*, 18, 1016–1022.

Egger, J., Hoinka, K.P. and Spengler, T. (2015) Aspects of potential vorticity fluxes: climatology and impermeability. *Journal of the Atmospheric Sciences*, 72, 3257–3267.

Ertel, H. (1942) Ein neuer hydrodynamischer Wirbelsatz. *Meteorology Zeitschr Braunschweigs*, 59, 271–281.

Garny, H. and Randel, W.J. (2013) Dynamic variability of the Asian monsoon anticyclone observed in potential vorticity and correlations with tracer distributions. *Journal of Geophysical Research: Atmospheres*, 118, 13421–13433.

Haynes, P.H. and McIntyre, M.E. (1987) On the evolution of vorticity and potential vorticity in the presence of diabatic heating and frictional or other forces. *Journal of the Atmospheric Sciences*, 44, 828–841.

Haynes, P.H. and McIntyre, M.E. (1990) On the conservation and impermeability theorems for potential vorticity. *Journal of the Atmospheric Sciences*, 47, 2021–2031.

Held, I.M. and Ting, M. (1990) Orographic versus thermal forcing of stationary waves: the importance of the mean low-level wind. *Journal of the Atmospheric Sciences*, 47, 495–500.

Held, I.M. and Schneider, T. (1999) The surface branch of the zonally averaged mass transport circulation in the troposphere. *Journal of the Atmospheric Sciences*, 56, 1688–1697.

Holton, J.R. (2004) *An Introduction to Dynamic Meteorology*. Cambridge, Massachusetts: Academic Press.

Hoskins, B.J., McIntyre, M.E. and Robertson, A.W. (1985) On the use and significance of isentropic potential vorticity maps. *Quarterly Journal of the Royal Meteorological Society*, 111, 877–946.

Hoskins, B.J. (1991) Towards a PV-θ view of the general circulation. *Tellus*, 43, 27–35.

Hoskins, B.J. and Rodwell, M.J. (1995) A model of the Asian summer monsoon. Part I: the global scale. *Journal of the Atmospheric Sciences*, 52, 1329–1340.

Hoskins, B.J., Pedder, M.D. and Jones, W. (2003) The omega equation and potential vorticity. *Quarterly Journal of the Royal Meteorological Society*, 129, 3277–3303.

Hsu, C.J. and Plumb, R.A. (2000) Nonaxisymmetric thermally driven circulations and upper-tropospheric monsoon dynamics. *Journal of the Atmospheric Sciences*, 57, 1255–1276.

Kanamitsu, M., Ebisuzaki, W., Woollen, J.S., Yang, S., Hnilo, J.J., Fiorino, M. and Potter, G. (2002) NCEP-DOE AMIP-II reanalysis (R-2). *Bulletin of the American Meteorological Society*, 83, 1631–1643.

Koshyk, J. and McFarlane, N. (1996) The potential vorticity budget of an atmospheric general circulation model. *Journal of the Atmospheric Sciences*, 53, 550–563.

Liu, Y., Wang, Z., Zhuo, H. and Wu, G. (2017) Two types of summertime heating over Asian large-scale orography and excitation of potential-vorticity forcing II. Sensible heating over Tibetan-Iranian Plateau. *Science China Earth Sciences*, 60, 733–744.

Liu, S., Wu, Q., Schroeder, S.R., Yao, Y., Zhang, Y., Wu, T., Wang, L. and Hu, H. (2020a) Near-global atmospheric responses to observed springtime Tibetan plateau snow anomalies. *Journal of Climate*, 33, 1691–1706.

Liu, Y., Lu, M., Yang, H., Duan, A., He, B., Yang, S. and Wu, G. (2020b) Land-atmosphere-ocean coupling associated with the Tibetan Plateau and its climate impacts. *National Science Review*, 7, 534–552.

Lu, M., Yang, S., Li, Z., He, B., He, S. and Wang, Z. (2018) Possible effect of the Tibetan Plateau on the "upstream" climate over West Asia, North Africa, South Europe and the North Atlantic. *Climate Dynamics*, 51, 1485–1498.

Lu, M., Yang, S., Wang, J., Wu, Y. and Jia, X. (2021) Response of regional Asian summer monsoons to the effect of reduced surface albedo in different Tibetan Plateau domains in idealized model experiments. *Journal of Climate*, 34, 7023–7036.

Lutsko, N.J., Baldwin, J. and Cronin, T. (2019) The impact of large-scale orography on northern hemisphere winter synoptic temperature variability. *Journal of Climate*, 32, 5799–5814.

Ma, T., Liu, Y., Wu, G., Mao, J. and Zhang, G. (2020) Effect of potential vorticity on the formation, development, and eastward movement of a Tibetan Plateau vortex and its influence on downstream precipitation. *Chinese Journal of Atmospheric Sciences*, 44(3), 472–486 (in Chinese).

Ma, T., Wu, G., Liu, Y. and Mao, J. (2022) Abnormal warm sea-surface temperature in the Indian Ocean, active potential vorticity over the Tibetan Plateau, and severe flooding along the Yangtze River in summer 2020. *Quarterly Journal of the Royal Meteorological Society*, 148, 1001–1019.

Manabe, S. and Terpstra, T. (1974) The effects of mountains on the general circulation of the atmosphere as identified by numerical experiments. *Journal of the Atmospheric Sciences*, 31, 3–42.

McIntyre, M.E. (2015) Potential vorticity. In: *Encyclopedia of atmospheric sciences*, Vol. 2, 2nd edition., Amsterdam: Elsevier; pp. 375–383.

Nan, S., Zhao, P. and Chen, J. (2019) Variability of summertime Tibetan tropospheric temperature and associated precipitation anomalies over the Central-Eastern Sahel. *Climate Dynamics*, 52, 1819–1835.

Park, H., Xie, S. and Son, S. (2013) Poleward stationary Eddy heat transport by the Tibetan Plateau and equatorward shift of westerlies during northern winter. *Journal of the Atmospheric Sciences*, 70, 3288–3301.

Plumb, R.A. and Hou, A. (1992) The response of a zonally symmetric atmosphere to subtropical thermal forcing: threshold behavior. *Journal of the Atmospheric Sciences*, 49, 1790–1799.

Plumb, R.A. and Ferrari, R. (2005) Transformed Eulerian-mean theory. Part I: Nonquasigeostrophic theory for eddies on a zonal-mean flow. *Journal of Physical Oceanography*, 35(2), 165–174.

Prein, A.F. and Heymsfield, A.J. (2020) Increased melting level height impacts surface precipitation phase and intensity. *Nature Climate Change*, 10, 771–776.

Rodwell, M. and Hoskins, B.J. (1996) Monsoons and the dynamics of deserts. *Quarterly Journal of the Royal Meteorological Society*, 122, 1385–1404.

Rossby, C.G. (1936) Dynamics of steady ocean currents in the light of experimental fluid mechanics. *Papers in physical oceanography and meteorology (published by Massachusetts Institute of Technology and Woods Hole Oceanographic Institution)*, 5(1), 1–43.

Rupp, P. and Haynes, P. (2021) Zonal scale and temporal variability of the Asian monsoon anticyclone in an idealised numerical model. *Weather and Climate Dynamics*, 2, 413–431.

Schneider, T., Held, I.M. and Garner, S.T. (2003) Boundary effects in potential vorticity dynamics. *Journal of the Atmospheric Sciences*, 60, 1024–1040.

Schneider, T. (2005) Zonal momentum balance, potential vorticity dynamics, and mass fluxes on near-surface Isentropes. *Journal of the Atmospheric Sciences*, 62(6), 1884–1900.

Schneider, T., Bischoff, T. and Haug, G.H. (2014) Migrations and dynamics of the intertropical convergence zone. *Nature*, 513, 45–53.

Sheng, C., Wu, G., Tang, Y., He, B., Xie, Y., Ma, T., Ma, T., Li, J., Bao, Q. and Liu, Y. (2021) Characteristics of the potential vorticity and its budget in the surface layer over the Tibetan Plateau. *International Journal of Climatology*, 41, 439–455.

Son, J., Seo, K. and Wang, B. (2019) Dynamical control of the Tibetan Plateau on the east Asian summer monsoon. *Geophysical Research Letters*, 46, 7672–7679.

Sun, R., Duan, A., Chen, L., Li, Y., Xie, Z. and Zhao, Y. (2019) Interannual variability of the North Pacific mixed layer associated with the spring Tibetan Plateau thermal forcing. *Journal of Climate*, 32, 3109–3130.

Škerlak, B., Sprenger, M., Pfahl, S., Tyrlis, E. and Wernli, H. (2015) Tropopause folds in ERA-interim: global climatology and relation to extreme weather events. *Journal of Geophysical Research: Atmospheres*, 120, 4860–4877.

Wang, G., He, Y., Huang, J., Guan, X., Wang, X., Hu, H., Wang, S. and Xie, Y. (2022) The influence of precipitation phase changes on the recharge process of terrestrial water storage in the cold season over the Tibetan Plateau. *Journal of Geophysical Research: Atmospheres*, 127, e2021JD035824.

Wu, G. (1984) The nonlinear response of the atmosphere to large-scale mechanical and thermal forcing. *Journal of the Atmospheric Sciences*, 41, 2456–2476.

Wu, G. and Liu, H. (1997) Vertical vorticity development owing to down-sliding at slantwise isentropic surface. *Dynamics of Atmospheres and Oceans*, 27, 715–743.

Wu, G. and Liu, Y. (2000) Thermal adaptation, overshooting, dispersion, and subtropical anticyclone part I: thermal adaptation and overshooting. *Chinese Journal of Atmospheric Sciences*, 24(4), 433–446 (in Chinese).

Wu, G. and Liu, Y. (2003) Summertime quadruplet heating pattern in the subtropics and the associated atmospheric circulation. *Geophysical Research Letters*, 30, 1201.

Wu, G., Liu, Y., Wang, T., Wan, R., Liu, X., Li, W., Zhang, Z., Zhang, Q., Duan, A. and Liang, X. (2007) The influence of mechanical and thermal forcing by the Tibetan Plateau on Asian climate. *Journal of Hydrometeorology*, 8, 770–789.

Wu, G., Liu, Y., He, B., Bao, Q., Duan, A. and Jin, F. (2012) Thermal controls on the Asian summer monsoon. *Scientific Reports*, 2, 404.

Wu, G., He, B., Liu, Y., Bao, Q. and Ren, R. (2015a) Location and variation of the summertime upper-troposphere temperature maximum over South Asia. *Climate Dynamics*, 45, 2757–2774.

Wu, Z., Zhang, P., Chen, H. and Li, Y. (2015b) Can the Tibetan Plateau snow cover influence the interannual variations of Eurasian heat wave frequency? *Climate Dynamics*, 46, 3405–3417.

Wu, G., Zhuo, H., Wang, Z. and Liu, Y. (2016) Two types of summertime heating over the Asian large-scale orography and excitation of potential-vorticity forcing I. over Tibetan Plateau. *Science China Earth Sciences*, 59, 1996–2008.

Wu, G., Ma, T., Liu, Y. and Jiang, Z. (2020) PV-Q perspective of cyclogenesis and vertical velocity development downstream of the Tibetan Plateau. *Journal of Geophysical Research: Atmospheres*, 125, e2019JD030912.

Xie, Y., Wu, G., Liu, Y. and Huang, J. (2020) Eurasian cooling linked with Arctic warming: insights from PV dynamics. *Journal of Climate*, 33, 2627–2644.

Xie, Y., Wu, G., Liu, Y., Huang, J. and Nie, H. (2022) A dynamic and thermodynamic coupling view of the linkages between Eurasian cooling and Arctic warming. *Climate Dynamics*, 58, 2725–2744.

Yanai, M. and Wu, G. (2006) Effects of the Tibetan Plateau. In: *The Asian Monsoon*. Berlin, Heidelberg: Springer Praxis Books. https://doi.org/10.1007/3-540-37722-0_13.

Yang, H., Shen, X., Yao, J. and Wen, Q. (2020) Portraying the impact of the Tibetan Plateau on global climate. *Journal of Climate*, 33, 3565–3583.

Yeh, T. (1950) The circulation of the high troposphere over China in the winter of 1945–46. *Tellus A*, 2, 173–183.

You, Q., Wu, T., Shen, L., Pepin, N.C., Zhang, L., Jiang, Z., Wu, Z., Kang, S. and Aghakouchak, A. (2020) Review of snow cover variation over the Tibetan Plateau and its influence on the broad climate system. *Earth-Science Reviews*, 201, 103043.

Zhao, P., Zhou, Z. and Liu, J. (2007) Variability of Tibetan spring snow and its associations with the hemispheric extratropical circulation and east Asian summer monsoon rainfall: an observational investigation. *Journal of Climate*, 20, 3942–3955.

Zhao, P., Xu, X., Chen, F., Guo, X., Zheng, X., Liu, L., Hong, Y., Li, Y., La, Z., Peng, H., Zhong, L., Ma, Y., Tang, S., Liu, Y., Liu, H., Li, Y., Zhang, Q., Hu, Z., Sun, J., Zhang, S., Dong, L., Zhang, H., Zhao, Y., Yan, X., Xiao, A., Wan, W., Liu, Y., Chen, J., Liu, G., Zhaxi, Y. and Zhou, X. (2017) The third atmospheric scientific experiment for understanding the earth–atmosphere coupled system over the Tibetan Plateau and its effects. *Bulletin of the American Meteorological Society*, 99, 757–776.

Zheng, Y., Wu, G. and Liu, Y. (2013) Dynamical and thermal problems in vortex development and movement. Part I: A PV-Q view. *Acta Meteorologica Sinica*, 27, 1–14.

SUPPORTING INFORMATION

Additional supporting information can be found online in the Supporting Information section at the end of this article.